Multi-Frequency Higher-Order ADI-FDTD Solvers for Signal Integrity Predictions and Interference Modeling in General EMC Applications

Nikolaos V. Kantartzis

Department of Electrical and Computer Engineering, Faculty of Technology
Aristotle University of Thessaloniki, GR-54124 Thessaloniki, Greece
kant@auth.gr

Abstract ─ The precise and wideband modeling of electromagnetic interferences and their effect on the signal integrity of microwave structures is presented in this paper, via an efficient 3-D dispersion-optimized method. Introducing a novel frequency-dependent alternating-direction implicit finite-difference time-domain algorithm in general curvilinear coordinates, the technique establishes a consistent multi-frequency higher-order stencil management formulation. Moreover, for arbitrary geometric discontinuities and abrupt curvatures, a field projection scheme is devised. Thus, the detrimental dispersion errors of existing approaches are drastically minimized and time-steps can now greatly exceed the stability condition at any frequency range. The proposed method leads to affordable simulations and very accurate results, as proven by a variety of electromagnetic compatibility problems.

Index Terms ─ EMC analysis, EMI prediction, higher-order ADI-FDTD methods, signal integrity.

I. INTRODUCTION

An essential issue in the electromagnetic compatibility (EMC) realization of modern electronic equipment is the fulfillment of certain immunity and emission standards. To this aim, the role of electromagnetic interference (EMI) is deemed critical since it can seriously affect the signal integrity of most microwave devices. Actually, this issue has become the topic of a constant research for the design of proficient components with the highest possible sensitivity and confined intermodulation distortions [1-11]. Considering that these structures may receive many expensive reconfigurations before their final form, the need for a cost-effective and robust approach offering fast and rigorous EMI estimations, is indeed of major importance. However, this task is rather cumbersome, especially on a broadband basis, as most of the devices have a lot of geometric details, arbitrary discontinuities, or involve dispersive materials which call for fine meshes and prolonged simulations. For these difficulties to be overcome, the combination of the alternating-direction implicit (ADI) concept with the finite-difference time-domain (FDTD) method [12] can be proven a powerful means [13, 14]. Nonetheless, extensive studies revealed that the original algorithm suffers from rapidly growing dispersion errors as time-steps increase, a fact that led to several noteworthy algorithms for its correction [15-25].

The key objective of this paper is the development of an accuracy-adjustable class of dispersion-reduction ADI-FDTD solvers for the enhanced analysis of signal integrity and EMI interactions in contemporary EMC applications. Being fully wideband, the 3-D algorithm associates new higher-order frequency-dependent spatial/temporal forms with optimal stencils that produce generalized dual curvilinear grids. Furthermore, for the manipulation of small-scale structural details or irregularities, a conformal field projection on preselected planes is introduced. On the other hand, to preserve consistency amid neighboring areas, a family of boundary and continuity conditions is employed to ensure smooth transition. In view of its controllable formal precision and unconditional stability, the multi-frequency technique provides certain advantages over conventional approaches. Particularly, it permits the choice of time-steps well above the Courant limit, without creating prohibitive dispersion artifacts and enables the construction of coarse, yet

sufficiently adaptable, lattices. Therefore, intermodulation deformations are thoroughly resolved and signal integrity is reliably estimated. These properties are numerically validated by an assortment of different EMC arrangements, like waveguides, resonators, cavities, junctions, specialized antennas, metamaterial structures, and anechoic/reverberation test facilities.

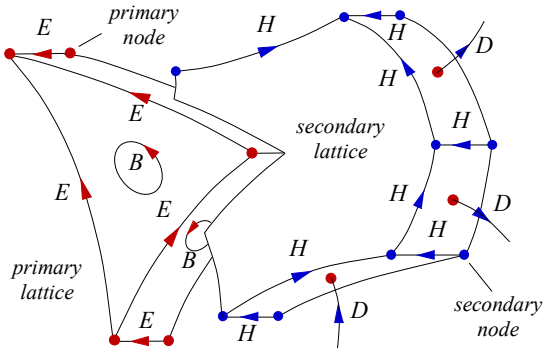

Fig. 1. Geometry of the dual mesh tessellation.

II. HIGHER-ORDER OPERATORS

The central contribution of our formulation focuses on the development of a high-precision non-orthogonal ADI-FDTD technique, whose actual performance – unlike several existing approaches – does not depend on dispersion errors as time-steps exceed the Courant limit. Moreover, the novel algorithm is intended to be fully generalized in terms of adaptive meshing, geometric details, and material modeling to successfully simulate all intricate wave interactions without needing excessive computational resources.

A. Discretization and dual-lattice construction

Starting from the correct interpretation of the underlying physical problem, the proposed discretization framework is based on highly-accurate spatial/temporal interpolation schemes and dual adaptive grids, as those of Fig. 1. More specifically, the construction of these meshes is based on the selection of the appropriate coordinate system that leads to cells of optimal quality [24-27]. To this aim, we start with an adaptive primary lattice, whose refinement is conducted according to the geometric details of the structures, under study, and the achievement of the minimum reflection error at neighboring cell interfaces. This local refinement process on the primary grid yields a finite number of uniquely defined local patterns [28, 29], which, if properly assembled at their adjacent vertices, enable the formation of an equally consistent secondary grid (see Fig. 1). Next and via a dual mesh notion, magnetic field **H** components are placed at secondary edge centers, to remain in absolute staggering with electric field **E** components located at primary edge centers [30-32]. Note that all quantities required for the update of the proposed algorithm are evaluated through a field flux concept across cell faces [7] which preserves the hyperbolic nature of Maxwell's equations and saves a lot of numerical effort.

B. Accuracy-controllable operators

Let us assume a general coordinate system (u,v,w) defined by the corresponding $g(u,v,w)$ metrical coefficients, which describe all of its implementation issues. In our formulation, spatial and temporal derivatives are evaluated by a new Lth-order accurate operator, whose expressions are, respectively, given by

$$S_\eta\left[f\big|_{u,v,w}^{t}\right]=\frac{e^{L\Delta\eta/4}}{\sqrt{\pi}\Delta\eta}Q_\eta^L\left[f\big|_{u,v,w}^{t}\right]+\sum_{s=1}^{3}\left(1+\frac{\Delta\eta}{4s}\right)f\big|_{\eta\pm s\Delta\eta}^{t}, \quad (1)$$

$$\mathcal{T}\left[f\big|_{u,v,w}^{t}\right]=\frac{1}{\Phi(\Delta t)}\left(f\big|_{u,v,w}^{t+\Delta t/2}-f\big|_{u,v,w}^{t-\Delta t/2}\right)-q\frac{\partial^3 f}{\partial t^3}\bigg|_{u,v,w}^{t}, \quad (2)$$

where $\eta\in(u,v,w)$, $\Delta\eta\in(\Delta u,\Delta v,\Delta w)$ is the spatial increment and Δt the time-step. Parameter q controls the impact of extra nodes due to higher-order derivatives [7, 10]. After some algebra, one obtains

$$q=(a+2)(\Delta\eta)^{L-1}-(a-1)(\Delta\eta)^{L}, \quad (3)$$

for $a\in[0,1]$ being a weighting coefficient relative to the frequency spectrum of our approximation.

Proceeding to the analysis of (1), special attention must be drawn to the contribution of the novel multi-frequency operator $Q_\eta[.]$. Its extra degree of freedom D denotes the suitable stencil size and introduces auxiliary nodes that allow the satisfactory modeling of abrupt waves or fine geometric details. In particular,

$$Q_\eta^L\left[f\big|_{u,v,w}^{t}\right]=\frac{g(u,v,w)}{\Psi(k_\eta\Delta\eta)}\sum_{l=1}^{L}Y_l\left\{\sum_{d=1}^{D}V_{l,d}\left[f\big|_{u,v,w}^{t}\right]\right\}. \quad (4)$$

Coefficients Y_l (with a total sum of 1/2) improve grid consistency, primarily in signal integrity estimations, whereas correction functions $\Phi(\Delta t)$ and $\Psi(k_\eta\Delta\eta)$ of (2) and (4), enhance the accuracy of derivative approximation. In wideband EMI simulations, which are rather demanding for most time-domain schemes, these functions are proven very

effective. Essentially, they consider the excitation frequency content and subdue all oscillatory modes that can corrupt propagating waves. Note that for low-frequency applications, where strong coupling phenomena occur, this behavior is retained, as well. Such an issue is deemed critical for EMC optimization due to the important influence of the excitation on the final design. In this context, function $\Psi(k_\eta\Delta\eta)$, with k_η the k_u, k_v, or k_w component of wavevector **k**, gives the best nodal pattern for the construction of the mesh. To acquire their arguments, the $\mathcal{S}_\eta\,[e^{jk\eta}]/\partial_\zeta e^{jk\eta} \rightarrow 1$ constraint should be satisfied, which in higher-order realizations becomes $\mathcal{S}_\eta\,[e^{jk\eta}]/\partial_\eta\, e^{jk\eta} \approx 2[\cos(k_\eta\Delta\eta) - 1]$; a strict requirement for minimizing dispersion errors, not easily achieved by traditional techniques [31]. So, suitable $k_\eta\Delta\eta$ are derived by the Fourier transform of already computed components at fixed positions near geometric details and the mean value of the estimated frequency spectrum. Herein, the two functions are selected to be the combination of exponential and hyperbolic terms

$$\Phi(\Delta t) = \frac{e^{\Delta t/2}}{2\Delta t - 3}\sinh\left[\Delta t\sqrt{1-(\Delta t/2)^2}\right], \tag{5}$$

$$\Psi(k_\eta\Delta\eta) = e^{5\sqrt{2p-1}}\Delta\eta\cosh\left(\Delta\eta\sqrt{p+2}\right), \tag{6}$$

with $p = k_\eta\Delta\eta/2$. To complete the theoretical description, operators $V_{l,d}[.]$, in (4), must be defined. Basically, they are responsible for the combination of the nodal patterns introduced by (4). In contrast to Yee's method that involves only two lattice points for derivative computation, the specific scheme employs a complete set of nodes which yield coarse but very robust grids [34]. A typical w-directed (for $D = 5$) $V_{l,d}[.]$ operator receives the compact expression of

$$V_{l,d}\left[f\big|^t_{u,v,w}\right] = \frac{(\Delta w)^l}{5l+1} \times\sum_{r=-1}^{+1}\left[f\big|^t_{u-\Delta u,v+\Delta v,w+r\Delta w} - f\big|^t_{u+\Delta u,v-\Delta v,w-r\Delta w}\right]. \tag{7}$$

The purpose of r is the consistent treatment of regions near perfectly electric conducting outer walls or composite media interfaces, i.e. cases where stencils extend at least two nodes on each side of a mesh point.

Observing the multi-frequency algorithm, presented above, it is stated that (1), (2), (4), and (7) launch a class of 3-D higher-order spatial and temporal forms with advanced dispersion-reduction assets. In fact, it is the structural consistency of (4) and (7) that increases the overall performance. Consequently, the latter operators subdue the typical discretization defects created during the modeling of most microwave structures and especially of electrically large ones. Moreover, their auxiliary nodes guarantee the correct representation of laborious geometries, so evading severe inaccuracies [30-34]. Given that lengthy propagation paths in several EMC setups are related to multiple interactions from compound interfaces, the extraction of wideband update formulas is expected to be a considerable contribution. However, one must be aware of the regularly encountered discontinuities with non-zero tangential quantities that demand notable overheads. This is, also, drastically alleviated by (1)-(7), which, except for their superior precision, can be applied to frequency-dependent problems. Thus, in the next sections, we extract novel unconditionally-stable expressions, able to offer an optimal phase velocity, mainly independent of lattice reflection errors.

III. GENERALIZED ADI-FDTD ALGORITHM

For the development of the frequency-dependent methodology, one must start from magnetic, $\mathbf{B} = [B_u, B_v, B_w]^T$, and electric, $\mathbf{D} = [D_u, D_v, D_w]^T$, flux densities

$$\mathbf{B} = \mu(\omega)\mathbf{H} = \mu_0\mathbf{H} + \mathbf{M}, \tag{8}$$

$$\mathbf{D} = \varepsilon(\omega)\mathbf{E} = \varepsilon_0\mathbf{E} + \mathbf{P}, \tag{9}$$

where $\mathbf{H} = [H_u, H_v, H_w]^T$, $\mathbf{E} = [E_u, E_v, E_w]^T$ represent magnetic and electric field intensities and $\mathbf{M} = [M_u, M_v, M_w]^T$, $\mathbf{P} = [P_u, P_v, P_w]^T$ the auxiliary magnetic and electric polarizations that consider the dispersive nature (Debye, Lorentz or Drude) of every material with constitutive parameters $\varepsilon(\omega)$, $\mu(\omega)$. Application of (1)-(7) to Faraday's and Ampere's laws, gives

$$\Xi^{\mathrm{E}}\mathcal{S}[\mathbf{E}] = -\mathcal{T}[\mathbf{B}], \tag{10}$$

$$\Xi^{\mathrm{H}}\mathcal{S}[\mathbf{H}] = \mathcal{T}[\mathbf{D}] + \sigma\mathbf{E} + \mathbf{J}, \tag{11}$$

where σ denotes the electric losses, $\mathbf{J} = [J_u, J_v, J_w]^T$ is the electric current density source used for external excitation, and $\Xi^{\mathrm{E,H}}$ are 3×3 dual metric tensors whose elements, expressed as functions of $g(u,v,w)$, characterize the (u,v,w) coordinate system selected for our analysis. On the other hand, $\mathcal{S} = [\mathcal{S}_u\ \mathcal{S}_v\ \mathcal{S}_w]^T$ is the non-orthogonal curl operator, described by

$$\mathcal{S}[.] = \mathrm{CURL}[.] = \begin{bmatrix} 0 & -S_w & S_v \\ S_w & 0 & -S_u \\ -S_v & S_u & 0 \end{bmatrix}. \quad (12)$$

The proposed ADI-FDTD algorithm retains the simplicity of the common approach [13-18] and circumvents the defects of regular finite-difference configurations. Thus, it divides the original iteration of a component into two sub-iterations, namely, for time forwarding from the nth to the $(n + 1)$th time-step, we get: the first sub-iteration from n to $n + 1/2$ and the second one from $n + 1/2$ to $n + 1$. It is emphasized that for the sake of symmetry during the ADI splitting process, the electric current density terms in (11) are replaced with judiciously adjusted temporal averages. For instance, at time-step $n + 1/2$,

$$\sigma \mathbf{E}^{n+1/2} = \sigma\left[(\mathbf{E}^{n+1/2} + \mathbf{E}^{n}) + (\mathbf{E}^{n+1} + \mathbf{E}^{n+1/2})\right]/4, \quad (13)$$

$$\mathbf{J}^{n+1/2} = (\mathbf{J}^{n+1/4} + \mathbf{J}^{n+3/4})/2, \quad (14)$$

from which the $\sigma(\mathbf{E}^{n+1/2} + \mathbf{E}^{n})/4$, $\mathbf{J}^{n+1/4}/2$ terms belong to the first and the $\sigma(\mathbf{E}^{n+1} + \mathbf{E}^{n+1/2})/4$, $\mathbf{J}^{n+3/4}/2$ terms to the second sub-iteration of the method. Let us, now, take into account the dual structure of Fig. 1 and focus on the unconditionally-stable update of the E_u component. In the first sub-iteration, the u-directed part of the dispersion-optimized Ampere's law, (11), yields

$$\mathcal{T}\left[D_u\big|_{\mathrm{A}}^{n+1/2}\right] + \frac{\sigma}{4}\left(E_u\big|_{\mathrm{A}}^{n+1/2} + E_u\big|_{\mathrm{A}}^{n}\right) + \frac{1}{2}J_u\big|_{\mathrm{A}}^{n+1/4} = \Xi_w^{\mathrm{H}} S_v\left[H_w\big|_{\mathrm{A}}^{n+1/2}\right] - \Xi_v^{\mathrm{H}} S_w\left[H_v\big|_{\mathrm{A}}^{n}\right], \quad (15)$$

with the subscript A = $(i + 1/2, j, k)$. Using (2) for the expansion of the temporal operator, one derives

$$D_u\big|_{\mathrm{A}}^{n+1/2} = D_u\big|_{\mathrm{A}}^{n} + \Phi(\Delta t)\left\{\Xi_w^{\mathrm{H}} S_v\left[H_w\big|_{\mathrm{A}}^{n+1/2}\right] - \Xi_v^{\mathrm{H}} S_w\left[H_v\big|_{\mathrm{A}}^{n}\right] - \frac{\sigma}{4}\left(E_u\big|_{\mathrm{A}}^{n+1/2} + E_u\big|_{\mathrm{A}}^{n}\right) - \frac{1}{2}J_u\big|_{\mathrm{A}}^{n+1/4} + \Lambda_D\right\}, \quad (16)$$

for Λ_D a weighting function that contains all higher-order (HO) temporal differentiations of D_u conducted at n or earlier time-steps [19-23]. Combined with the $\Phi(\Delta t)$ of (5) and the enhanced spatial operators, this extra degree of freedom leads to a large suppression of the dispersion mechanism, even when the Courant stability criterion has been appreciably exceeded.

As observed from (16), partial derivative $S_v[H_w]$ at $n + 1/2$ must be implicitly calculated, as it involves only unknown H_w values at A = $(i \pm 1/2, j + 1/2, k)$ nodes, while its $S_w[H_v]$ counterpart can be explicitly given by the already computed H_v quantities at the nth time-step. To eliminate H_w, the same ADI notion is implemented in the w-directed part of Faraday's law, (10), thus concluding to

$$\mu\mathcal{T}\left[H_w\big|_{\mathrm{B}}^{n+1/2}\right] = \Xi_u^{\mathrm{E}} S_v\left[E_u\big|_{\mathrm{B}}^{n+1/2}\right] - \Xi_v^{\mathrm{E}} S_u\left[E_v\big|_{\mathrm{B}}^{n}\right], \quad (17)$$

with B = $(i \pm 1/2, j \pm 1/2, k)$. Again, expanding $\mathcal{T}[.]$

$$H_w\big|_{\mathrm{B}}^{n+1/2} = H_w\big|_{\mathrm{B}}^{n} + \frac{\Phi(\Delta t)}{\mu}\left\{\Xi_u^{\mathrm{E}} S_v\left[E_u\big|_{\mathrm{B}}^{n+1/2}\right] - \Xi_v^{\mathrm{E}} S_u\left[E_v\big|_{\mathrm{B}}^{n}\right] + \Lambda_H\right\}, \quad (18)$$

in which Λ_H is the corresponding function for the HO temporal derivatives of H_w based on known data [34]. Nevertheless, prior to the use of (18), we will deal with the final unknown of (16), i.e. the D_u at $n + 1/2$, attributed to the presence of the frequency-dependent materials in the computational domain. To treat this term, an unconditionally-stable Crank-Nicolson technique, applied to (9) is employed. Hence,

$$P_u\big|_{\mathrm{A}}^{n+1/2} = \frac{\varepsilon_0\omega_0\Phi(\Delta t)}{4+\Phi(\Delta t)}\left(E_u\big|_{\mathrm{A}}^{n+1/2} + E_u\big|_{\mathrm{A}}^{n}\right) + \frac{4-\Phi(\Delta t)}{4+\Phi(\Delta t)}P_u\big|_{\mathrm{A}}^{n} + \frac{\Lambda_P}{4+\Phi(\Delta t)}, \quad (19)$$

where Λ_P is again the suitable weighting function. Now, plugging (18), (19) into (16) gives the update expression (20) for E_u at $n + 1/2$ (bottom of page). Parameters χ_m (for m = 1,2,…,9) are defined in terms of spatial increments, function $\Phi(\Delta t)$, material constitutive properties and metrical coefficients $g(u,v,w)$. Since, χ_m have constant values, their evaluation – hardly affecting the total burden – is conducted only once and utilized during the update of the particular field quantity. Repetition, of (20) for every j along the v mesh direction, where the spatial alternation occurs, yields a sparse 3-band tridiagonal system of equations that is recursively solved through well-known techniques [13-15]. Upon acquiring E_u, the prior formulation is identically applied to E_v and E_w, while magnetic and electric polarizations are explicitly obtained via their higher-order FDTD expressions.

The second sub-iteration for the time advancing of E_u in the interval from $n + 1/2$ to $n + 1$ reverses the roles of $S_v[H_w]$ and $S_w[H_v]$, modifying (14) as

$$\mathcal{T}\left[D_u\big|_{\mathrm{A}}^{n+1/2}\right]+\frac{\sigma}{4}\left(E_u\big|_{\mathrm{A}}^{n+1}+E_u\big|_{\mathrm{A}}^{n+1/2}\right)+\frac{1}{2}J_u\big|_{\mathrm{A}}^{n+3/4} =\Xi_w^{\mathrm{H}}S_v\left[H_w\big|_{\mathrm{A}}^{n+1/2}\right]-\Xi_v^{\mathrm{H}}S_w\left[H_v\big|_{\mathrm{A}}^{n+1}\right]. \quad (21)$$

The unknown variables, now, are H_v and D_u (after expanding $\mathcal{T}[.]$) at $n+1$. Eliminating these terms in a way similar to (17)-(19), one gets (22), shown below, with ψ_m the counterparts of χ_m. Once all electric quantities are computed, by solving the resulting systems, the remaining fields are explicitly evaluated and the algorithm continues with the next time-step.

A completely analogous strategy holds for media, whose frequency-dependent constitutive parameter is permeability μ. Notice, also, that the extension of the multi-frequency methodology to structures, comprising both types of dispersive media, is straightforward without any additional constraints.

$$\chi_1 E_u\big|_{i+1/2,j,k}^{n+1/2}-\chi_2 E_u\big|_{i+1/2,j+1,k}^{n+1/2}-\chi_3 E_u\big|_{i+1/2,j-1,k}^{n+1/2}=\chi_4 E_u\big|_{i+1/2,j,k}^{n}+\chi_5 J_u\big|_{i+1/2,j,k}^{n+1/4}+\chi_6 S_v\left[H_w\big|_{i+1/2,j+1/2,k}^{n}\right] -\chi_7 S_w\left[H_v\big|_{i+1/2,j,k+1/2}^{n}\right]-\chi_8\left\{S_u\left[E_v\big|_{i,j+1/2,k}^{n}\right]+S_v\left[E_u\big|_{i,j-1/2,k}^{n}\right]\right\}+\chi_9 P_u\big|_{i+1/2,j,k}^{n+1/2}, \quad (20)$$

$$\psi_1 E_u\big|_{i+1/2,j,k}^{n+1}-\psi_2 E_u\big|_{i+1/2,j,k+1}^{n+1}-\psi_3 E_u\big|_{i+1/2,j,k-1}^{n+1}=\psi_4 E_u\big|_{i+1/2,j,k}^{n+1/2}+\psi_5 J_u\big|_{i+1/2,j,k}^{n+3/4}-\psi_6 S_w\left[H_v\big|_{i+1/2,j,k+1/2}^{n+1/2}\right] +\psi_7 S_v\left[H_w\big|_{i+1/2,j+1/2,k}^{n+1/2}\right]+\psi_8\left\{S_v\left[E_w\big|_{i,j,k+1/2}^{n+1/2}\right]-S_w\left[E_v\big|_{i,j,k-1/2}^{n+1/2}\right]\right\}-\psi_9 P_u\big|_{i+1/2,j,k}^{n+1/2}, \quad (22)$$

Indeed, every material is rigorously modeled by the appropriate scheme regarding the variation of ε or μ [17]. Finally, it is important to stress that, aside from some limited storage needs, the novel procedure does not considerably increase the total CPU and memory requirements. On the contrary, its ability to accomplish dispersion-optimized simulations by letting temporal increments to be greatly augmented, leads to serious savings.

IV. STABILITY AND DISPERSION ANALYSIS

Pertaining to the stability of the proposed algorithm, the von Neumann method is applied [12]. Thus, the two sub-iterations are expressed in matrix form as

$$n \to n+1/2: \qquad \mathbf{Z}_1\mathbf{E}^{n+1/2}=\mathbf{\Theta}_1\mathbf{E}^{n}, \quad (23)$$

$$n+1/2 \to n+1: \qquad \mathbf{Z}_2\mathbf{E}^{n+1}=\mathbf{\Theta}_2\mathbf{E}^{n+1/2}, \quad (24)$$

where sparse matrices $\mathbf{Z}_l$, $\mathbf{\Theta}_l$ (for $l=1,2$) are created by the proper χ_m and ψ_m parameters during the rearrangement of the system of equations. If (23) and (24) are combined into a single equation, one obtains

$$\mathbf{E}^{n+1}=\mathbf{Z}_2^{-1}\mathbf{\Theta}_2\mathbf{Z}_1^{-1}\mathbf{\Theta}_1\mathbf{E}^{n}=\mathbf{K}\mathbf{E}^{n}. \quad (25)$$

The eigenvalues of matrix $\mathbf{K}$ are found to be

$$\rho_{1,2}=1, \quad \rho_\tau=\left[\sqrt{G_1^2-7G_2^2}\pm j\left(G_2/5-2G_1\right)\right]/5G_2, \quad (26)$$

for $\tau=3,\ldots,6$ and coefficients G_1, G_2 depending on $(\Delta t/\Delta\eta)\sin(k_\eta\Delta\eta/2)$. After the required mathematics, it is proven that the magnitudes of (26) are always less or equal to unity, thus certifying the initial convention for the algorithm. In this manner, Δt can be safely selected far beyond the Courant limit, without the prohibitive influence of the detrimental lattice errors, now, decisively suppressed up to 10 orders. Such a performance implies that the specific ADI-FDTD technique is fully conservative and of high convergence, since it subdues anisotropy errors, as well.

On the other hand, it would be very instructive to examine the improvement of the dispersion relation and verify the large suppression of the relevant error, mainly when the time-step is larger than that dictated by the conventional stability criterion. Following a general framework, the dispersion error is defined as

$$e_{disp}=F_{ex}(u,v,w,t)-F_{num}(u,v,w,t) =\int\alpha(\omega)e^{j\left[\mathbf{k}_{ex}(\omega)-\mathbf{k}_{num}(\omega)\right]\cdot\mathbf{r}}d\omega, \quad (27)$$

in which F_{ex} is the exact and F_{num} the numerical solution of the problem with their respective wavenumber vectors $\mathbf{k}_{ex}$ and $\mathbf{k}_{num}$. Functions $\alpha(\omega)$ are the amplitudes of the Fourier transform in (27), while $\mathbf{r}$

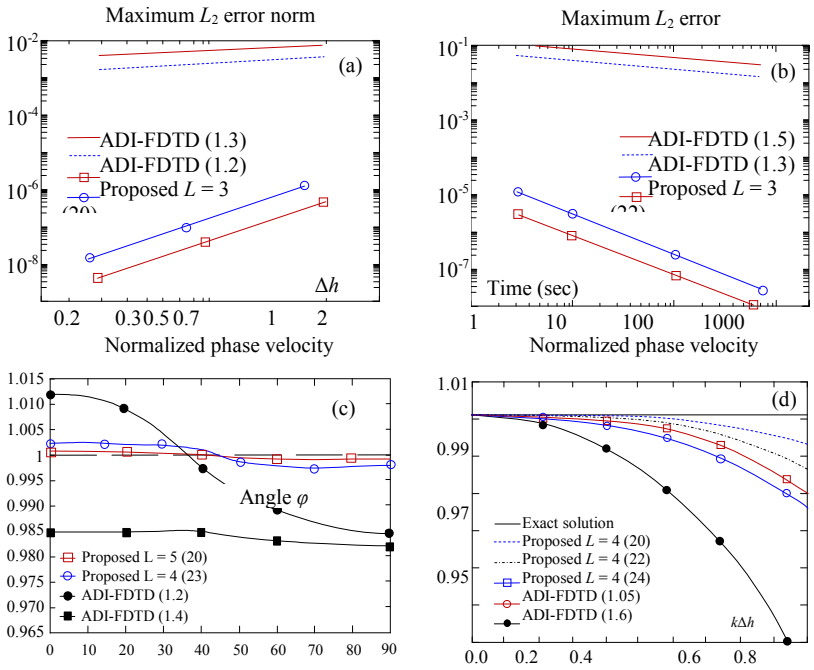

Fig. 2. Maximum L_2 error norm versus (a) spatial increment and (b) time. Normalized phase velocity versus (c) angle of propagation and (d) gridding density.

is a position vector in the (u,v,w) coordinate system. Note that F_{num} is the superposition of both propagating and evanescent waves. This idea is deemed more realistic, as it takes into account the strenuous evanescent waves that are customarily responsible for critical inaccuracies near discontinuities. In this context, the extraction of the dispersion error is based on the estimate of

$$\sum_{\zeta=u,v,w}\left|e^{j\left[k_{ex}(\omega)-k_{num}(\omega)\right]\zeta}\right| \le \sum_{\zeta=u,v,w}\left|k_{ex}(\omega)-k_{num}(\omega)\right|\left|\zeta\right|, \quad (28)$$

with $k_{ex}(\omega)=\omega$ the free-space dispersion relation and

$$k_{num}(\omega) \cong \omega\left\{1-\frac{2(\Delta t)^{L+3D}}{725}+O\left[(\Delta t)^{2L+3D}\right]\right\}, \quad (29)$$

the corresponding formula of the multi-frequency ADI-FDTD method. It is evident that (29) exhibits a significant enhancement, easily adjusted by the order of accuracy L and the complementary degree of freedom D. In the light of these considerations, e_{disp} becomes

$$e_{disp} \cong \frac{4+3(\Delta t)^{L+D}}{986}\omega\,. \quad (30)$$

To indicate the superiority of (29), for D = 3, over the typical ADI-FDTD dispersion relation, Fig. 2 presents the maximum L_2 error norm and the normalized phase velocity as a function of different parameters at a spectrum of 15 GHz. For notation compactness, we define the gauge CFLN = $\Delta t^{MT}/\Delta t^{FDTD}$ (MT = proposed or plain ADI-FDTD method) as the Courant-Friedrichs-Levy number, shown in parenthesis at the legend of every figure. Also, Table 1 summarizes the maximum dispersion error and the convergence rate of various implementations. Apparently, the higher-order methodology accomplishes a serious and wideband reduction of discretization errors, unlike the usual technique, whose performance deteriorates progressively as Δt depart from the stability condition. These benefits are more prominent for large CFLN, optimally handled by the pertinent L and D values.

Table 1: Maximum dispersion and convergence rate

Method	Grid density	Maximum dispersion	Convergence rate
ADI-FDTD (1.5)	1/40	3.84579	1.62412
ADI-FDTD (1.2)	1/25	2.465×10^{-1}	1.75679
FDTD (1.0)	1/15	1.532×10^{-2}	1.90304
Proposed L = 3 (18)	1/10	3.072×10^{-7}	3.18712
Proposed L = 5 (22)	1/9	5.068×10^{-10}	4.97021
Proposed L = 7 (25)	1/8	8.034×10^{-12}	7.01584

V. CURVED INTERFACE TREATMENT

The presence of curved media interfaces or geometric discontinuities with arbitrary cross sections in real-world EMC applications constitutes a principal modeling difficulty for the majority of numerical methods. Unfortunately, these geometric irregularities are proven detrimental for the simulation of EMI phenomena, since they arouse non-separable and highly oscillatory wavefronts that require extremely fine grid resolutions and excessive computational resources.

A. Dissimilar material boundaries

To retain consistency amid regions with media of different constitutive parameters, a set of continuity conditions with optimal sensitivity is developed. The process launches an adaptive concept, which employs extra nodes at both interface sides, in the area of node P, and follows the variation of the curvature as

$$\frac{1}{\varepsilon_1}\left(\sum_{real} s_{1,j} + \sum_{extra} s_{2,j}\right) = \frac{1}{\varepsilon_2}\left(\sum_{extra} s_{1,j} + \sum_{real} s_{2,j}\right), \quad (31)$$

where 1,2 are the dissimilar media, s differencing weights at real or extra nodes, and j the stencil for the summation around P [28-30]. Therefore, all sub-wavelength details are accurately tracked, while their contribution is directly integrated in Maxwell's equations in an exploitable form. This manipulation offers high levels of reliability and smooth regional transition without unexpected instabilities.

B. Irregular cross-sections and discontinuities

Presume the complex cross-section of Fig. 3, stretching over an angle θ_D with inner and outer mean

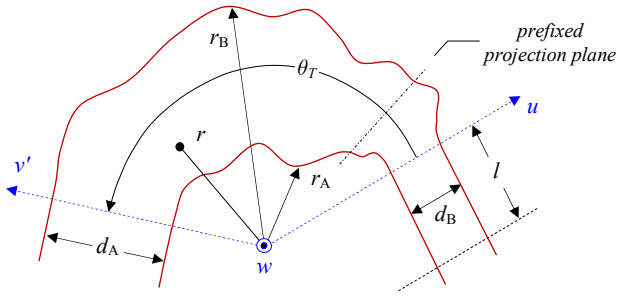

Fig. 3. An arbitrary geometric discontinuity.

radii r_1 and r_2. For its treatment, we separate every propagating mode at κ prefixed transverse planes, which satisfy all physical continuity conditions.

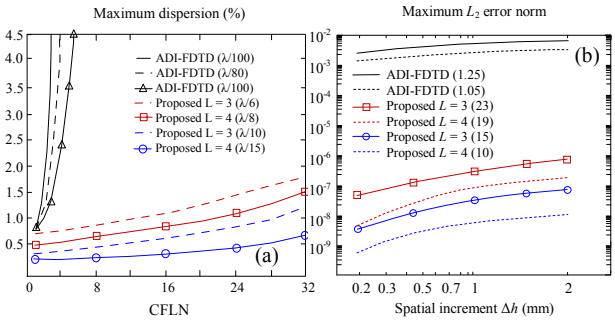

Fig. 4. (a) Maximum dispersion and (b) maximum L_2 norm variation for the parallel-plate waveguide.

Hence, each component f, defined at a local (ρ, θ, φ) system, can be expressed as

$$f(r,\theta,\varphi) = \sum\nolimits_{\kappa} \zeta_{\kappa} F_{\kappa}(r,\theta,\varphi), \quad (32)$$

with $$\zeta_{\kappa} = \frac{2}{r_M}\cos\left[\kappa\pi\left(\frac{r-r_1}{r_M}\right)\right],$$

$r_M = r_2 - r_1$, ζ_κ the corresponding eigenfunctions and F_κ known amplitude coefficients [3, 7]. The new scheme is purely conformal and provides consistent meshes via the choice of r_1, r_2. Two effectively smooth functions that fulfill this goal, with $\alpha_{\theta,\varphi} = (\theta - \varphi)/\theta_D$, $d = d_2 - d_1$, and $d_2 = 1.5d_1$, are

$$r_1 = d\left(\alpha_{\theta,\varphi} - 1.65\right) + d_1 - 0.45d_2, \quad (33)$$

$$r_2 = -d\left(\alpha_{\theta,\varphi} - 1.75\right) + 0.2d_1 + 0.35d_2. \quad (34)$$

After the prior mode decoupling, the next step is the projection of Maxwell's laws on the prefixed κ planes to obtain our differential equation model. Each solution is considered as a transverse intermediate excitation surface in the discontinuity. This approach maintains lattice quality near the geometric details, contrary to other renditions that cannot supply equivalent outcomes. In this way and using a matrix notation, Ampere's and Faraday's laws locally become

$$\partial_t\left[\varepsilon(\omega)\mathbf{E}\right] = \left(\mathbf{U}^{\mathrm{A}} + \mathbf{U}^{\mathrm{B}}\mathbf{U}^{\mathrm{C}}\right)\nabla\times\mathbf{H} - \mathbf{U}^{\mathrm{D}}\mathbf{P}, \quad (35)$$

$$\partial_t\left[\mu(\omega)\mathbf{H}\right] = -\mathbf{U}^{\mathrm{C}}\nabla\times\mathbf{E} + \mathbf{U}^{\mathrm{D}}\mathbf{H} - \mathbf{U}^{\mathrm{E}}\mathbf{M}, \quad (36)$$

in which all spatial and temporal derivatives are evaluated by means of (1) and (2). Also, the elements of $\mathbf{U}^i$ (i = A,…,E) structural matrices include the main mesh details in the vicinity of the cross-section, while their values are given by

$$U^{\mathrm{A}}_{\kappa\lambda} = (-1)^{\kappa+2\lambda}\kappa^2/\left(\kappa^2+\lambda^2\right), \qquad U^{\mathrm{B}}_{\kappa\lambda} = \kappa^2\lambda^2 - 1,$$

$$U^{\mathrm{C}}_{\kappa\lambda} = r_1 + d/2, \qquad U^{\mathrm{D}}_{\kappa\lambda} = \kappa r_M - \lambda d/4,$$

$$U_{\kappa\lambda}^{\mathrm{E}} = (-1)^{2\kappa+\lambda} r_2 / \left(\kappa^2 + \lambda^2\right).$$

In fact, a careful choice of κ, improves the multi-frequency behavior of the entire method.

VI. NUMERICAL VERIFICATION

To substantiate the advantages of our method, we, start from a set of simple examples for which analytical solutions exist. Thus, proving its accuracy and numerical dispersion reduction capabilities, we will, then, proceed to more realistic EMC applications.

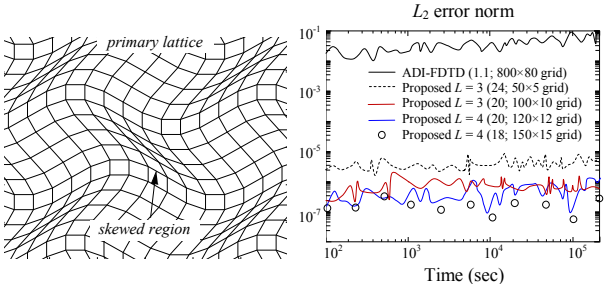

Fig. 5. Temporal variation of the L_2 norm for the parallel-plate waveguide discretized by a skewed mesh.

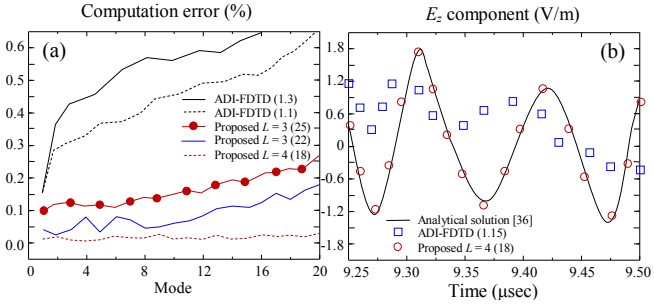

Fig. 6. (a) Computation error and (b) variation of the E_z component for the 3-D rectangular cavity.

The first test problem explores the propagation of the TM_1 mode in a parallel-plate 0.5×5.5 m waveguide. For the entire simulation, excitation and boundary field values – obtained from the analytical solution [35] – are assigned to both ports, while the device is truncated by a 12-cell perfectly matched layer [12]. The waveguide is highly elongated and, hence, considerable dispersion errors are expected to appear when employing traditional approaches or exceeding the Courant limit. Using various non-uniform grid sizes, ranging from 10×150 to 30×1200 cells, simulations are conducted until steady-state is attained. Figure 4a gives the maximum dispersion (%) versus CFLN; while, Fig. 4b gives the maximum L_2 error norm with respect to the spatial step. The large dispersion errors of the usual ADI-FDTD method as CFLN increase along with the superiority of the proposed technique are promptly discernible for all lattice resolutions.

Table 2: Resonant frequencies of the cylindrical dielectric cavity with $\varepsilon_r = 3.8$

Exact [35] (GHz)	Method	Comp. (GHz)	Error (%)	Maximum Dispersion
TE_{111} 9.896	ADI-FDTD	9.454	4.467	2.532×10^{-1}
	Proposed	9.894	0.011	5.471×10^{-11}
TM_{010} 11.235	ADI-FDTD	10.557	6.031	9.031×10^{-1}
	Proposed	11.231	0.035	8.964×10^{-11}
TM_{011} 12.211	ADI-FDTD	11.328	7.228	1.548
	Proposed	12.204	0.052	2.109×10^{-10}
TE_{112} 13.028	ADI-FDTD	11.776	9.605	3.042
	Proposed	13.019	0.068	7.286×10^{-10}
TM_{012} 14.899	ADI-FDTD	13.201	11.397	6.751
	Proposed	14.886	0.083	9.047×10^{-10}
TE_{211} 15.085	ADI-FDTD	12.843	14.862	8.984
	Proposed	15.068	0.107	4.103×10^{-9}

Additionally, the previous waveguide is revisited by means of a skewed mesh (Fig. 5) to examine the behavior of the new schemes in the case of discretization discontinuities responsible for several types of inaccuracies. From the outcomes of Fig. 5, illustrating the temporal variation of the local error and different orders of accuracy L, one can, easily, derive that our schemes remain very precise, even for large CFLN, unlike the existing second-order implementation.

Next, we move to some broadband problems and particularly to the computation of the first 20 resonant modes of a 3-D air-filled cavity with perfectly conducting walls. The modes are derived through a fast Fourier transform of the computed signals at prefixed locations. Figure 6a shows the error (%) of our calculations and Fig. 6b presents a comparison between the simulated and analytical waveform [36]. As observed, the conventional

Table 3: Maximum L_2 error for the TE_{11} mode

Lattice	ADI-FDTD	CPU time	Proposed	CPU time
10×5×90	68.43129	5.2 m	0.20421	17.35 s
32×16×288	24.58074	26.3 m	0.04372	1.46 m
56×28×504	16.04823	2.43 h	0.00347	7.72 m
78×39×702	3.94618	6.57 h	0.00025	21.89 m

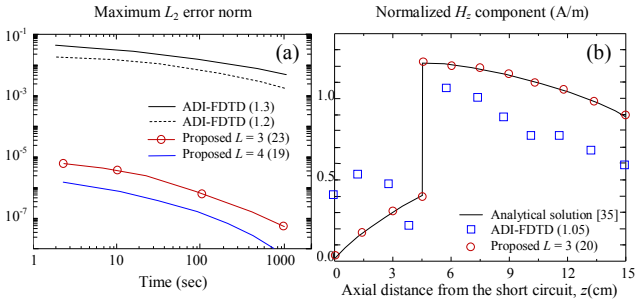

Fig. 7. (a) Maximum L_2 error norm and (b) normalized E_z component for the lossy-slab waveguide.

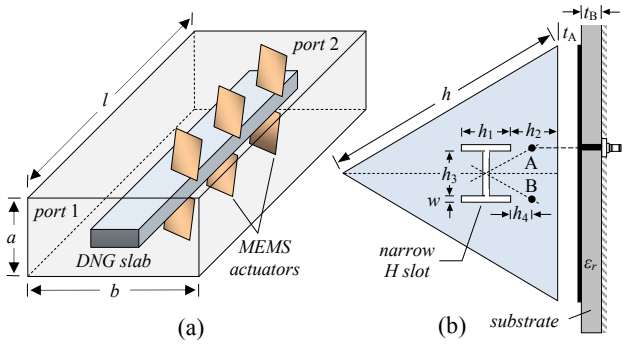

Fig. 8. (a) An RF MEMS-based coaxial waveguide and (b) a triangular H-slot microstrip antenna.

Table 4: Resonances of the coaxial waveguide

Ref. [8] (GHz)	Method	Comp. (GHz)	Error (%)	CPU Time	Maximum Dispersion
3 Actuators 11.781	ADI-FDTD	10.777	8.52	12.5 h	1.792×10^{-1}
	Proposed	11.779	0.01	51 m	3.082×10^{-11}
4 Actuators 14.205	ADI-FDTD	12.903	9.16	11.9 h	3.981
	Proposed	14.201	0.03	45 m	5.483×10^{-10}
5 Actuators 16.423	ADI-FDTD	14.647	10.81	10.9 h	6.432
	Proposed	16.235	0.05	36 m	3.561×10^{-10}

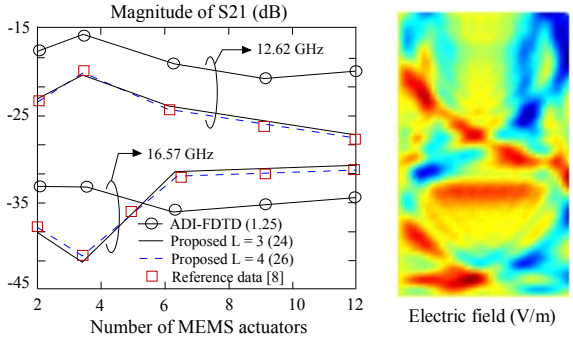

Fig. 9. Magnitude of the S_{21}-parameter versus the MEMS number and an electric field snapshot.

ADI-FDTD method lacks to provide reliable results, while our technique is, again, proven very efficient. In a similar manner, analysis moves to a parallel-plate cylindrical dielectric (ε_r = 3.8) resonator with a height of 15.75 mm and a radius of 5.35 mm. Table 2 gives the first six resonant frequencies of the structure obtained via the usual staircase ADI-FDTD method (CFLN = 1.16; grid: 180×180×360) and the proposed algorithm (CFLN = 18, L = 3; grid: 40×40×80). Herein, the conformal profile of the latter scheme leads to a 10-order dispersion error reduction.

Remaining in waveguides, let us, now, examine a 3-D air-filled 0.5×0.25×0.8 cm rectangular structure. The analytical solution [36] is inserted at the z = 0.8 cm port at all time steps together with the initial conditions. Using diverse lattices, Table 3 sums up the dispersion errors for the computation of the TE_{11} mode, from which the acceleration and the high accuracy of the enhanced method are deduced. Analogous conclusions are drawn from Fig. 7 for the same waveguide which, now, has a lossy ($\mu_r = 2 - j2$) slab with a length of 0.27 cm along the z axis. Note the inability of the regular ADI-FDTD scheme to model the material discontinuity in contrast to the new technique.

Having certified the performance of our methodology, we then investigate various realistic EMC setups in terms of EMI behavior and signal integrity prediction. Their selection has been mainly based on complexity, fine details, and electrical size. In fact such issues cannot be adequately manipulated by the usual staircase ADI-FDTD method either due to its insufficient discretization models or the need for prohibitively elongated steady-state simulations. All infinite domains are truncated by a modified 8-cell perfectly matched layer [12], while the results, whenever possible, are compared with reference/measurement data.

The first application is the coaxial waveguide of Fig. 8a, which involves a set of microelectromechanical (MEMS) actuators for selective mode propagation. Its inner slab is based on a double negative (DNG) metamaterial, described by a Drude model and the basic dimensions are: l = 11 mm, a = 1.7 mm, and b = 6.2 mm. The choice of such a problem is primarily attributed to the increasing use of complicated MEMS and DNG setups in several high-end arrangements. Table 4 gives the resonance frequencies for three cases (with L = 3) and several realizations. Moreover, the

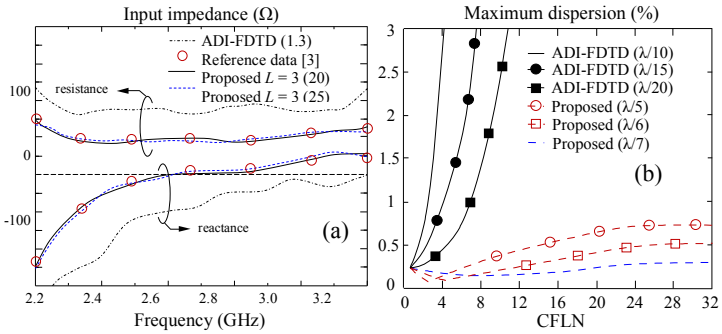

Fig. 10. (a) Input impedance and (b) maximum dispersion error for the *H*-slot microstrip antenna.

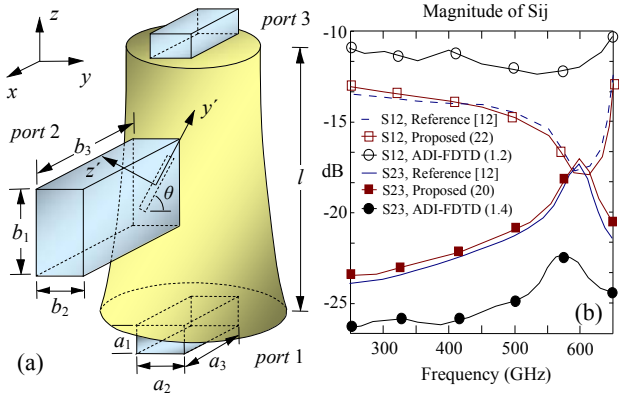

Fig. 11. (a) An inclined-slot three-port junction and (b) magnitude of *S*-parameters versus frequency.

variation of the S_{21}-parameter versus MEMS number is presented in Fig. 9 along with an indicative electric field snapshot directly above the actuators. It appears that, the proposed ADI-FDTD schemes are quite accurate and economical, attaining greatly diminished dispersion errors for large CFLN selections.

Subsequently, let us focus on the equilateral triangular *H*-slot microstrip (ε_r = 4.3) antenna of Fig. 8b, encountered in many up-to-date communication systems. Its dimensions are: h = 40 mm, h_1 = 12.2 mm, h_2 = 10.1 mm, h_3 = 12.8 mm, h_4 = 5.5 mm, t_A = 6.2 mm, t_B = 1.58 mm, and w = 1.2 mm. Figure 10a gives the input impedance, while Fig. 10b presents the maximum dispersion error versus CFLN for diverse resolutions. Note that the plain ADI-FDTD method (grid: 260×282×74; 62000 time-steps), cannot cope with this problem. Conversely, the optimized schemes are proven workable (81% coarser mesh and a maximum lattice reflection error of 2.398×10^{-10}), without the excessive CPU requirements of the usual algorithm.

Proceeding to the signal integrity of waveguide

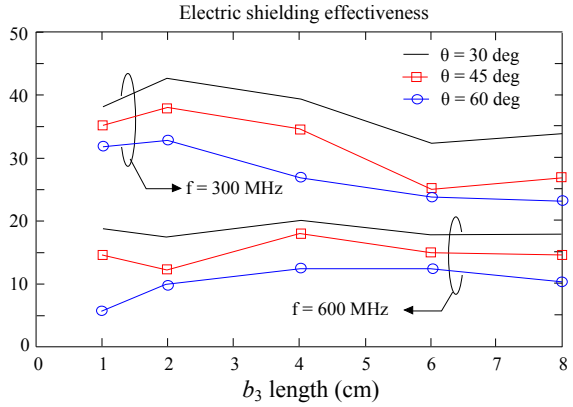

Fig. 12. Shielding effectiveness of the aperture.

junctions – a popular item in EMC applications – the next problem examines the elliptical cavity of Fig. 11a, which has a sidewall inclined slot, coupled to a rectangular waveguide. Typical dimensions are: a_1 = 6.52 mm, a_2 = 11.22 mm, a_3 = 21.35 mm, b_1 = 23.64 mm, b_2 = 11.52 mm, and l = 68.74 mm. For L= D = 3, in (1) and (3), the domain is discretized into 24×38 ×116 cells. Figure 11b gives the magnitude of two *S*-parameters, while Fig. 12 illustrates

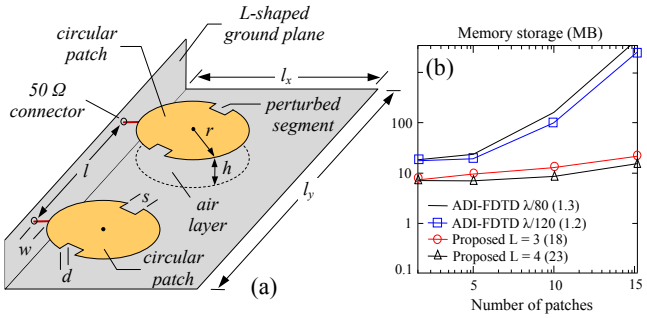

Fig. 13. (a) A wideband patch array and (b) memory storage versus the number of circular patches.

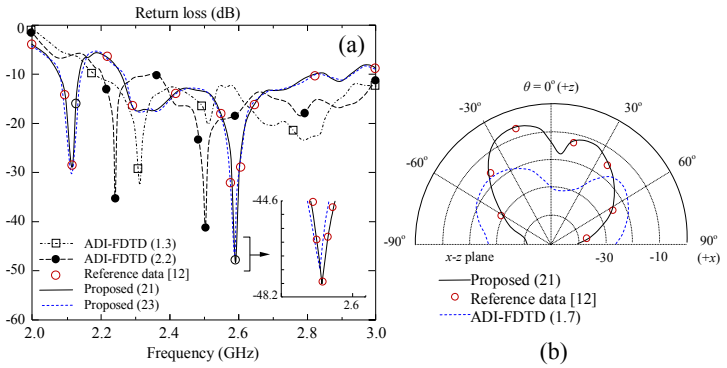

Fig. 14. (a) Return loss and (b) radiation pattern for the wideband 2×1 patch array.

the shielding effectiveness for diverse inclinations of the coupling slot and lengths of the b_3 side. As can be deduced, the enhanced ADI-FDTD technique – unlike its staircase counterpart – is able to manipulate this demanding simulation, even though the curved parts comprise a relatively large portion of the computational domain.

We, now, investigate the 2×1 patch array of Fig. 13a, with its cross-polarized profile attained by two perturbed segments (0.74% of the patch). Due to its frequent use in many systems, the optimal design of such an antenna will require a reliable simulation tool. Its dimensions are: l_x = 110 mm, l_y = 316 mm, r = 22 mm, l = 32 mm, h = 0.17 mm, w = 3.6 mm, d = 2.6 mm, and s = 5.7 mm. The mesh employs 68×110×26 cells (L = 3, D = 2), unlike the regular 91% larger grid. To verify the cost-effective profile of the new algorithm, Fig. 13b provides its memory needs versus the number of circular patches. As observed, its overhead remains relatively stable and in very low levels considering the complexity of the problem. Conversely, the usual ADI-FDTD method is proven far more expensive, especially above the typical value of 5 patches. Also, Fig. 14 shows the return loss and radiation pattern at 3.4 GHz. Again, our technique agrees very well with the reference data [3, 12] (actual accuracy: 0.0028% to 0.0032%), despite the large CFLN. In fact, this attains a dispersion error practically 9 orders of magnitude lower than the usual ADI-FDTD one (actual accuracy: 6.5312% to 8.9124%).

To this end, analysis moves to the coaxial four-port microwave splitter with a 2.4×0.8×0.6 mm DNG region (Fig. 15a). The outer conductor's cross-section is 6.3×5.7 mm and the inner's 1.3×0.9 mm. Figure 15b displays the return loss between ports 1 and 4, while Fig. 15c gives the variation of two S-parameters with regard to the number of used switches. Obviously, the wideband algorithm has a better performance for significantly lower CPU time, as indicated in Fig. 15d.

With regard to the modeling of electrically-large facilities, the next application is the inclined-wall dual reflector compact range anechoic chamber of Fig. 16. Being extremely expensive to construct, any effort toward the accurate estimation of its design parameters becomes really essential. Its

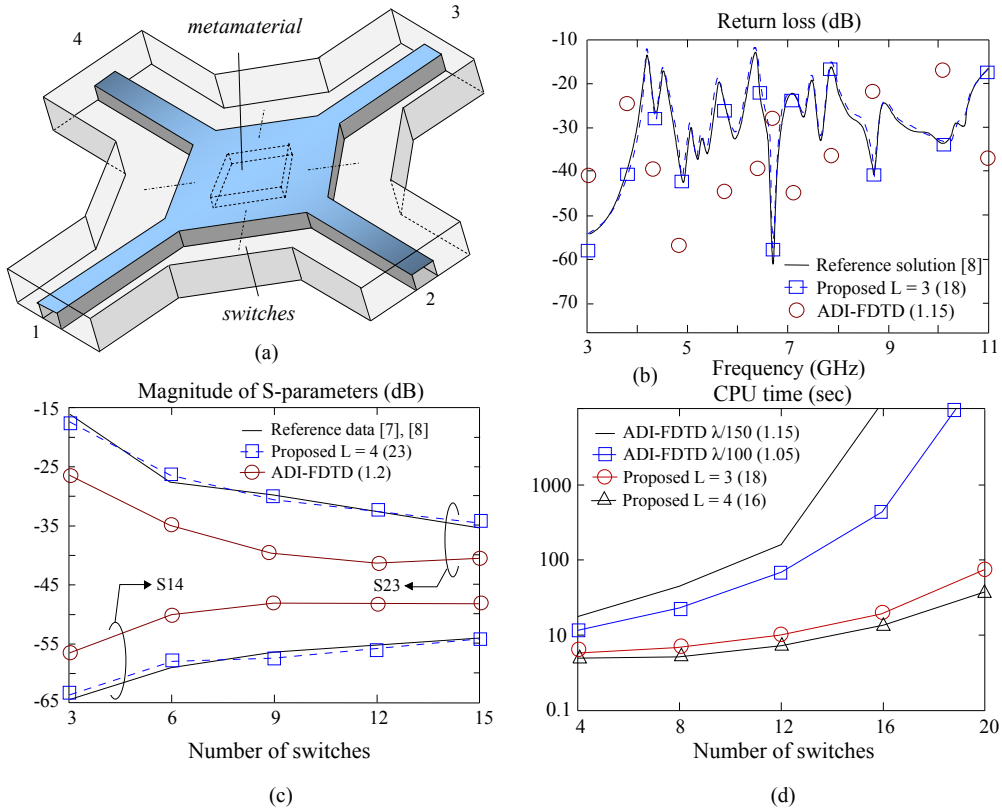

Fig. 15. (a) Geometry, (b) return loss, (c) magnitude of *S*-parameters, and (d) CPU time for a four-port microwave splitter with a DNG-based core.

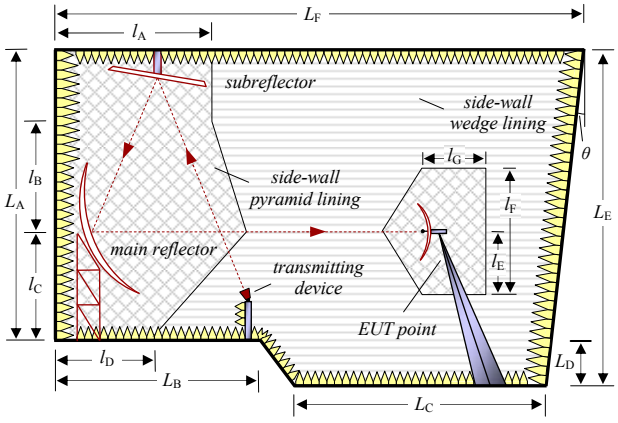

Fig. 16. A dual-reflector compact range anechoic chamber with an inclined rear wall.

width is 6.8 m, whereas L_A = 5.9 m, L_B = 4.1 m, L_C = 5.2 m, L_D = 1.5 m, L_E = 7.4 m, and L_F = 10.5 m. The diameters of the sub- and main reflector are 2.5 m and 3.9 m. Moreover, $\theta = 6^o$, l_A = 3.4 m, l_B = 2.6 m, l_C = 2.3 m, l_D = 2.1 m, l_E = 1.4 m, l_F = 2.8 m, and l_G = 1.3 m. The chamber is lined with different types of pyramids and wedges (Fig. 17b). Figure 17a presents the normalized site- attenuation of the facility's semi-anechoic version. Results indicate that notwithstanding its fine lattice, the simple ADI-FDTD method lacks to estimate the chamber's measurement suitability in contrast to our method which achieves an 85% overhead decrease. Similar outcomes are derived from Fig. 18, where the suitability of the facility's fully anechoic version is estimated. Notice, also, the impact of wedges on the performance of the semi-anechoic chamber in Fig. 19.

Finally, the signal integrity and EMI immunity of two nested reverberation chambers (Fig. 20) is analyzed. Their walls are covered by quadratic residue diffusers, i.e. a set of periodical phase gratings that diffract waves in extra directions. The movement of both stirrers is modeled with an interval of 20^o, while for each of their positions 60 time instants are sampled. The larger chamber has a length of 4.8 m, l_A = 3.72, l_B = 4.0 m and the smaller one a length of 2.44 m, l_C = 1.34 m, l_D= 1.78 m, with an aperture size of 0.32 m × 0.32 m. Figure 21 displays the shielding effectiveness of an 1.5 mm fiber-glass-fiber plate and a dielectric (ε_r = 3.4) cover. Once

more, our technique leads to very sufficient and wideband results, without critical dispersion errors due to high CFLN values.

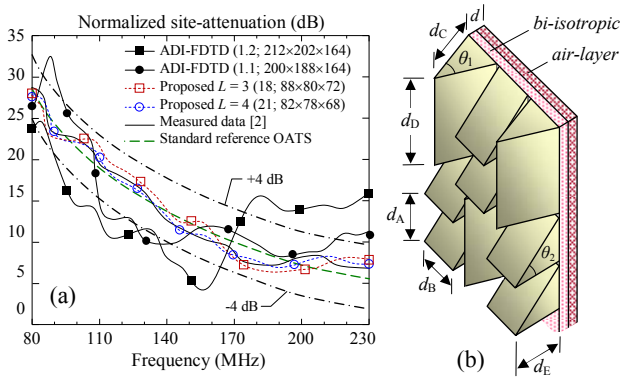

Fig. 17. (a) Normalized site-attenuation and (b) part of the absorptive wedges of the compact range chamber.

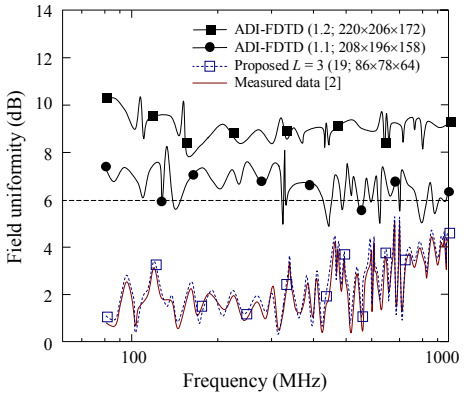

Fig. 18. Field uniformity of compact range facility .

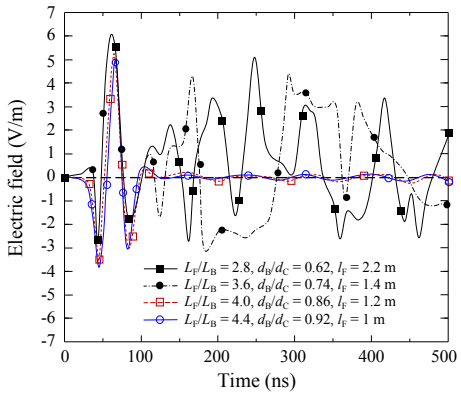

Fig. 19. Electric field variation in the compact range chamber for different structural parameters.

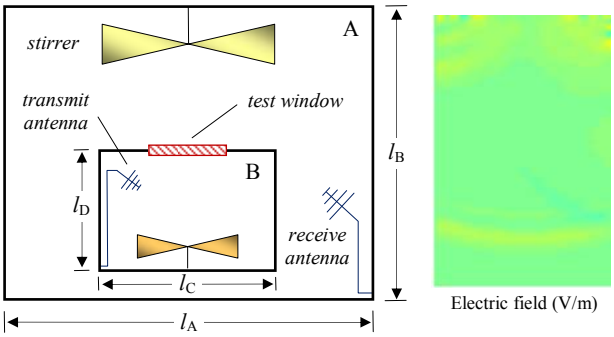

Fig. 20. A nested reverberation test facility along with a snapshot of the electric field near its wall diffusers.

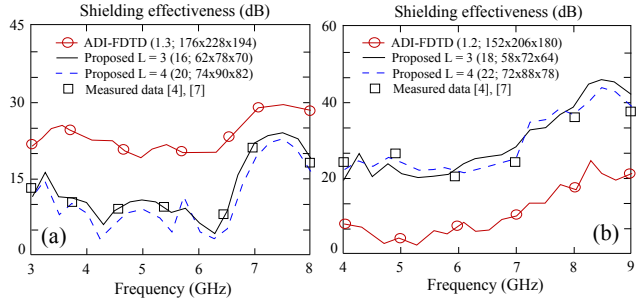

Fig. 21. Shielding effectiveness of (a) a 1.5 mm fiber-glass-fiber plate and (b) a dielectric (ε_r = 3.4) cover.

VII. CONCLUSION

A rigorous EMI analysis and signal integrity estimation of general EMC structures has been performed in this paper. To this aim, a new 3-D frequency-dependent higher-order ADI-FDTD method, incorporating a multi-frequency field projection scheme with an enhanced curvilinear nodal density, has been introduced and applied to a variety of problems, extending from waveguides, resonators, and antennas to large-scale test facilities. Their numerical simulations lead to very accurate and cost-effective realizations, even for coarse meshes and temporal increments that amply supersede the Courant stability condition.

REFERENCES

[1] C. Buccella, M. Feliziani, F. Maradei, and G. Manzi, "Magnetic field computation in a physically large domain with thin metallic shields," *IEEE Trans. Magn.*, vol. 41, no. 2, pp. 1708-1711, May 2005.

[2] C. Holloway, P. McKenna, R. Dalke, R. Perala, and C. Devor, "Time-domain modeling, characteriza-

tion, and measurements of anechoic and semi-anechoic electromagnetic test chambers," *IEEE Trans. Electromagn. Compat.*, vol. 44, no. 1, pp. 102-118, Feb. 2002.

[3] S. Lee, M. Vouvakis, and J.-F. Lee, "A non-overlapping domain decomposition method with non matching grids for modeling large finite arrays," *J. Comp. Phys.*, vol. 203, no. 1, pp. 1-21, Feb. 2005.

[4] C. Bruns and R. Vahldieck, "A closer look at reverberation chambers – simulation and experimental verification," *IEEE Trans. Electromagn. Compat.*, vol. 47, pp. 612-26, 2005.

[5] M. Sarto and A. Tamburrano, "Innovative test method for the shielding effectiveness measurement of thin films in wide frequency range," *IEEE Trans. Electromagn. Compat.*, vol. 48, no. 2, pp. 331-341, May 2006.

[6] Y. Song, N. Nikolova, and M. Bakr, "Efficient time-domain sensitivity analysis using coarse grids," *ACES J.*, vol. 23, no. 1, pp. 5-15, Mar. 2008.

[7] N. Kantartzis and T. Tsiboukis, *Modern EMC Analysis Techniques: Models and Applications*, Morgan & Claypool Publishers, San Rafael, CA, 2008.

[8] J. Muldavin, C. Bozler, S. Rabe, P. Wyatt, and C. Keast, "Wafer-scale packaged RF MEMS switches," *IEEE Trans. Microw. Theory Tech.*, vol. 56, pp. 522-529, Feb. 2008.

[9] S. Barmada, A. Gaggelli, P. Masini, A. Musolino, R. Rizzo, and M. Tucci, "Modeling of UIC cables in railway systems for their use as power line communication channels," *ACES J.*, vol. 24, no. 6, pp. 609-617, 2009.

[10] T. Ohtani, K. Taguchi, T. Kashiwa, Y. Kanai, and J. Cole, "Scattering analysis of large-scale coated cavity using the complex nonstandard FDTD method with surface impedance boundary condition," *IEEE Trans. Magn.*, vol. 45, no. 3, pp. 1296-1299, Mar. 2009.

[11] K. El Mahgoub, T. Elsherbeni, F. Yang, A. Elsherbeni, L. Sydänheimo, and L. Ukkonen, "Logo-antenna based RFID tags for advertising application," *ACES J.*, vol. 25, no. 3, pp. 174-181, Mar. 2010.

[12] A. Taflove and S. Hagness, *Computational Electrodynamics: The Finite-Difference Time-Domain Method*., Artech House, Norwood, MA, 2005.

[13] T. Namiki, "A new FDTD algorithm based on ADI method," *IEEE Trans. Microwave Theory Tech.*, vol. 47, no. 10, pp. 2003-2007, Oct. 1999.

[14] F. Zheng, Z. Chen, and J. Zhang, "An FDTD method without the Courant stability conditions," *IEEE Microw. Guided Wave Lett.*, vol. 9, no. 11, pp. 441-443, Nov. 1999.

[15] J. Mao, L. Jiang, and S. Luo, "Numerical formulations and applications of the ADI-FDTD method," *ACES Newsletter*, vol. 16, no. 3, pp. 12-18, Nov. 2001.

[16] M. Darms, R. Schuhmann, H. Spachmann, and T. Weiland, "Dispersion and asymmetry effects of ADI-FDTD," *IEEE Microw. Wireless Compon. Lett.*, vol. 12, pp. 491-493, 2002.

[17] S. Staker, C. Holloway, A. Bhobe, and M. Piket-May, "ADI formulation of the FDTD method: Algorithm and material dispersion implementation," *IEEE Trans. Electromagn. Compat.*, vol. 45, no. 2, pp. 156-166, May 2003.

[18] G. Sun and C. Truemann, "Efficient implementations of the Crank-Nicolson scheme for the FDTD method," *IEEE Trans. Microw. Theory Tech.*, vol. 54, no. 5, pp. 2275-84, May 2006.

[19] Erping Li, I. Ahmed, and R. Vahldieck, "Numerical dispersion analysis with an improved LOD–FDTD method," *IEEE Microw. Wireless Compon. Lett.*, vol. 17, pp. 319-321, 2007.

[20] E. Tan and D. Heh, "ADI-FDTD method with fourth order accuracy in time," *IEEE Microw. Wireless Compon. Lett.*, vol. 18, no. 5, pp. 296-298, May 2008.

[21] W. Fu and E. Tan, "Effective permittivity scheme for ADI-FDTD method at the interface of dispersive media," *ACES J.*, vol. 22, no. 2, pp. 120-125, June 2008.

[22] K. Jung, F. Teixeira, S. Garcia, and R. Lee, "On numerical artifacts of the complex envelope ADI-FDTD method," *IEEE Trans. Antennas Propag.*, vol. 57, pp. 491-498, Feb. 2009.

[23] Y. Zhang, S. Lu, and J. Zhang, "Reduction of numerical dispersion of 3-D higher order ADI-FDTD method with artificial anisotropy," *IEEE Trans. Microw. Theory Tech.*, vol. 57, no. 10, pp. 2416-28, Oct. 2009.

[24] H. Zheng and K. Leung, "A nonorthogonal ADI-FDTD algorithm for solving 2-D scattering problems," *IEEE Trans. Antennas Propag.*, vol. 57, no. 12, pp. 3981-3902, Dec. 2009.

[25] H. Zheng, L. Feng, and Q. Wu, "3-D nonorthogonal ADI-FDTD algorithm for the full-wave analysis of microwave circuit devices," *IEEE Trans. Microw. Theory Tech.*, vol. 58, no. 1, pp. 128-135, Jan. 2010.

[26] J.-F. Lee, R. Palendech, and R. Mittra, "Modeling three-dimensional discontinuities in waveguides using the nonorthogonal FDTD algorithm," *IEEE Trans. Microw. Theory Tech.*, vol. 40, no. 2, pp. 346-352, Feb. 1992.

[27] W. Yu, R. Mittra, and S. Dey, "Application of the nonuniform FDTD technique to analysis of coaxial discontinuity structures," *IEEE Trans. Microw. Theory Tech.*, vol. 49, pp. 207-209, Jan. 2001.

[28] S. Noelle, W. Rosenbaum, and M. Rumpf, "3D adaptive central schemes: Part I. Algorithms for assembling the dual mesh," *Appl. Numer. Math.*, vol.

56, no. 2, pp. 778-799, June 2006.
[29] P. Wang, "Modeling material responses by arbitrary Lagrangian Eulerian formulation and adaptive mesh refinement method," *J. Comput. Phys.*, vol. 229, pp. 1573-1599, Mar. 2010.
[30] R. Nilavalan, I. Craddock, and C. Railton, "Quantifying numerical dispersion in non-orthogonal FDTD meshes," *IEE Proc. Microw. Antennas Propag.*, vol. 149, pp. 23-27, 2002.
[31] N. Kantartzis and T. Tsiboukis, "A higher-order non-standard FDTD-PML method for the advanced modeling of complex EMC problems in generalized 3-D curvilinear coordinates," *IEEE Trans. Electromagn. Compat.*, vol. 46, no. 1, pp. 2-11, Feb. 2004.
[32] D. Firsov, J. LoVetri, O. Jeffrey, V. Okhmatovski, C. Gilmore, and W. Chamma, "High-order FVTD on unstructured grids using an object-oriented computational engine," *ACES J.*, vol. 22, no. 1, pp. 71-82, Mar. 2007.
[33] M. Hadi, "Wide-angle absorbing boundary conditions for low and high-order FDTD algorithms," *ACES J.*, vol. 24, no. 1, pp. 9-15, Feb. 2009.
[34] N. Kantartzis, T. Tsiboukis, and E. Kriezis, "An explicit weighted essentially non-oscillatory time-domain algorithm for the 3-D EMC applications with arbitrary media," *IEEE Trans. Magn.*, vol. 42, pp. 803-806, 2006.
[35] J. van Bladel, *Electromagnetic Fields*, IEEE Press, New York, NJ, 2007.
[36] D. Pozar, *Microwave Engineering*, John Wiley & Sons, New York, NJ, 2005.

Nikolaos V. Kantartzis received the Diploma and Ph.D. degrees from the Department of Electrical and Computer Engineering, Aristotle University of Thessaloniki, Greece, in 1994 and 1999, respectively. In 2001, he joined the same department, as a Postdoctoral Research Fellow, where, currently, he serves as an Assistant Professor. He has authored/co-authored 3 books, more than 50 referenced journals and over 60 conference papers. His main research interests include computational electromagnetics, EMC modeling, higher-order methods, metamaterials, and advanced microwave structures.